Full paper

Unravelling additive-based nanocrystal pinning for high efficiency organic-inorganic halide perovskite light-emitting diodes

Min-Ho Park[a,1], Su-Hun Jeong[a,1], Hong-Kyu Seo[a,1], Christoph Wolf[a], Young-Hoon Kim[b], Hobeom Kim[a], Jinwoo Byun[a], Joo Sung Kim[b], Himchan Cho[b], Tae-Woo Lee[b,c,*]

[a] Department of Materials Science and Engineering, Pohang University of Science and Technology (POSTECH), Pohang, Gyungbuk 790-784, Republic of Korea
[b] Department of Materials Science and Engineering, Seoul National University, 1 Gwanak-ro, Gwanak-gu, Seoul 08826, Republic of Korea
[c] Research Institute of Advanced Materials, Seoul National University, 1 Gwanak-ro, Gwanak-gu, Seoul 08826, Republic of Korea

ARTICLE INFO

ABSTRACT

Organic-inorganic halide perovskite light emitting diode (PeLED) as a narrow band emitter is an emerging research field. To overcome limited electroluminescence efficiency of PeLEDs, trap-assisted non-radiative recombination in polycrystalline perovskite films should be reduced and the electron-hole balance in the PeLEDs must be improved. In this work, we investigated a practical way to effectively overcome above-mentioned issues by unravelling additive-based nanocrystal pinning (A-NCP) process using the carefully controlled electron transporting organic material solutions diluted in a volatile non-polar solvent. We found that without affecting the intrinsic crystal structure, A-NCP improved the radiative recombination rate by reducing effective defect density at grain boundaries due to the defect healing effect. Moreover, it induced the improved electron-hole balance in the dominantly p-type $CH_3NH_3PbBr_3$ based PeLEDs, leading to the highest efficiency of 8.79% ever reported to date among organic-inorganic halide perovskite-based green PeLEDs. Therefore, our work gives the effective approaches for efficient PeLEDs from the investigations of the role of A-NCP incorporating a tiny amount of an electron transporting molecule as an additive to increase radiative recombination rate of polycrystalline perovskite films.

1. Introduction

Materials for light emitting diodes (LEDs) have been developed from inorganic materials to organic materials. Recently, solution-processable organic-inorganic halide ($CH_3NH_3MX_3$, CH_3NH_3 = methyl ammonium (MA), M = metal, X = halogen) perovskites (OHPs) have been dramatically developed for opto-electronic devices including solar cells and LEDs [1,2]. Compared to the active and vibrant researches for solar cell application, studies of LEDs are still at an infant stage due to the inherent physical characteristics of OHPs, which is more favorable for solar cells, including excellent optical absorption properties, high charge transport capability, long exciton diffusion lengths, and small exciton binding energy [1,2]. Nonetheless, efficient photoluminescence (PL) properties of OHP films have also been evaluated for use in LEDs [3–15]. The bandgap of OHP can be tuned by controlling its chemical composition, so OHPs can show electroluminescence (EL) in the visible range of spectrum [11,16]. The EL spectra have narrow full width at half maximum (≤ 20 nm), so OHPs have high color-purity. Therefore,

OHP LEDs (PeLEDs) are good candidates to replace conventional LEDs when the EL efficiency can be comparable with that of conventional organic LEDs.

Polycrystalline OHP films with large grains developed for solar cells have inherent disadvantages for LED application because of long exciton diffusion length, small exciton binding energy, and limited radiative recombination rate [17–20]. Overcoming these limitations is of critical importance to achieve highly efficient PeLEDs. First of all, thermal ionization and delocalization at room temperature in the OHP films due to small exciton binding energy (< 100 meV) and long exciton diffusion length (> 100 nm for pure OHP, > 1 μm for mixed halide OHP) is a facile process for exciton dissociation [11,19]. Enhancing exciton confinement in the small nanograins can be a good strategy so that reducing the grain sizes unlike the general strategy in OHP solar cells can be very effective to enhance PL and EL efficiency at the same time [15]. Secondly, in contrast to OHP solar cells, high radiative electron-hole recombination rate must be encouraged for the LED application [2,21]. In large perovskite grains, bulk recombination is

impeded by high carrier mobility and long charge diffusion length due to low defect density [2]. Therefore, low exciton recombination rate is inevitable in the OHP. Third, OHP polycrystals have defects including vacancies, interstitial elements, cation substitutions, and antisite substitutions [22,23]. These defects induce non-radiative recombination site by quenching excitons and trapping charges. Therefore, reducing the defect density in the OHP can increase the PL intensity and device efficiency. Lastly, to achieve high recombination rate in the emitting layer (EML) of LED, electrons and holes must be balanced effectively. OHP materials have dominantly p-type semiconducting properties, and MAPbBr$_3$ lacks n-doping behaviour [22,23]. The p-type electrical property of OHP leads to charge imbalance in the devices. Charge imbalance in p-type perovskite material can cause hole accumulation, which induces exciton-charge annihilation and low recombination rate [24]. Even though high radiative recombination rate and low defect density can be obtained in the OHP film, charge imbalance caused by the poorer electron transport than hole transport in the OHP EML and insufficient electron injection into the OHP EML from an organic electron transport layer (ETL) having lower electron mobility ($\mu_e = 10^{-6} - 10^{-3}$ cm^2 V^{-1} s^{-1} for electron transporting organic materials) than that of the OHP film ($\mu_e = 38$ cm^2 V^{-1} s^{-1} and 10^{-2} cm^2 V^{-1} s^{-1} for single crystal and spin-coated polycrystal, respectively) in devices significantly decreases EL efficiency [20,25,26]. Therefore, achieving efficient electron injection into a dominantly p-type perovskite EML and balanced charge transport in the EML would increase PeLED efficiency. At the current stage of research, it is quite required to develop a promising process or method to overcome these major limitations at the same time. We developed an additive-based nanocrystal pinning (A-NCP) process to make uniform nanograin films in which excitons are spatially confined well for higher recombination rates: this is emerging as a promising method to boost up the device efficiency [15]. However, the role of additive in the NCP process is unclear so that elucidation of the role of A-NCP is of urgent importance to boost up the efficiency further.

In this paper, we systemically investigated the role of A-NCP using an electron transporting small molecule as an additive that controls the nanograin size, reduces effective defect density of grain boundaries, and modifies surface coverage. It is simple but has a potential to overcome these limitations of conventional PeLEDs simultaneously. A-NCP effectively reduced the grain size of MAPbBr$_3$ significantly (~ 86.67 nm), and thereby achieved a relatively high recombination rate and low trap-assisted recombination rate by confining the excitons in the nanograins, reduced non-radiative recombination at grain boundaries by defect healing effect, and increased electrical characteristic of MAPbBr$_3$ film [15]. Moreover, A-NCP improved charge balance by effectively injecting electrons into the MAPbBr$_3$ EML and transporting electrons inside the MAPbBr$_3$ EML [22,23].

2. Experimental section

2.1. Sample preparation

A self-organized conducting polymer (SOCP) is composed of poly (3,4-ethylenedioxythiophene): poly(styrenesulfonate): perfluorinated ionomer (PEDOT:PSS (Clevios™ PVP AI4083): PFI = 1:6:25.4 (w:w:w)). A 50-nm-thick SOCP was spin-coated on a native silicon wafer or glass substrate, then annealed at 150 °C for 30 min. The samples were loaded into a N$_2$-filled glove box, then 40 wt% MAPbBr$_3$ solution (MABr (Solarmer) and PbBr$_2$ (Sigma Aldrich) in 1.06:1 M ratio in dimethyl sulfoxide (DMSO)) was spin-coated to form a 400-nm-thick EML. During MAPbBr$_3$ spin-coating process, its surface was treated by dropwise addition of solutions of 0, 0.03, 0.05, 0.07, and 0.1 wt% 1,3,5-tris(2-N-phenylbenzimidazolyl) benzene (TPBI) dissolved in chloroform (CF). After A-NCP process, 400-nm-thick MAPbBr$_3$ films were annealed at 90 °C for 10 min.

2.2. Film characterization

MAPbBr$_3$ surface was measured using a field-emission scanning electron microscope (SEM) (XL30S FEG, Philips electron optics B.V.). Crystal structure was defined using x-ray diffraction (XRD) (Rigaku, D/MAX-2500) and x-ray photoelectron spectroscopy (XPS) (Korea Basic Science Institute, photon source: monochromatic Al-Kα at 1486.6 eV). Radiative recombination rate and defect healing effects were investigated using steady-state PL (JASCO FP6500 spectrofluorometer with excitation wavelength of 405 nm); time-correlated single-photon counting (TCSPC) (PicoHarp 300 TCSPC module (PicoQuant GmbH)) which include a picosecond pulsed laser head (LDH-P-C-405B, PicoQuant, 405 nm excitation wavelength, ~ 150 fs pulse width) driven by a PLD800-D laser driver at 40-MHz repetition rate as excitation source equipped with a monochromator (SP-2155, Acton) and MCP-PMT (R3809U-50, Hamamatsu); and excitation-power-dependent PL by using the same source in continuous wave (CW) mode at 80 K and 300 K. PL spectra were collected using a Blue wave fiber-coupled spectrometer (StellarNET) with a resolution of 0.5 nm. Time-of-flight secondary ion mass spectroscopy (TOF-SIMS) experiments were performed with a TOF-SIMS 5 (ION-TOF GmbH, Münster, Germany) in the KBSI Busan Center by using a pulsed 30 keV Bi$^+$ primary beam with a current 0.64 pA. The analyzed area used in this work is a square of 200 μm × 200 μm. A negative ion spectra were internally calibrated using H$^-$, C$^-$, C$_2^-$, C$_3^-$ and C$_4^-$ peaks and a positive ion spectra were internally calibrated using H$^+$, CH^{3+}, C$_2$H$_5^+$, C$_3$H$_7^+$, C$_4$H$_9^+$ normalized to the respective secondary total ion yields. The chemical images of the analyzed area are recorded with 128×128 pixel resolution during the data acquisition. The depth profile is a square of 500 μm × 500 μm using Ar-cluster 5 KeV.

2.3. PeLEDs fabrication

Glass substrates were cleaned using acetone and isopropyl alcohol in ultrasonic bath for 15 min, respectively, and then dried at 80 °C in an oven. Glass substrates were treated with UVO cleaner for 15 min. SOCP was prepared by using PEDOT:PSS (Clevios™ PH500):PFI (1:2.5:11.2 (w:w:w)) solution with 5 wt% DMSO additive. Then 80-nm-thick SOCP was spin-coated and baked at 200 °C for 10 min, then was loaded in a N$_2$ filled glove box for deposition of a MAPbBr$_3$ EML by spin-coating. Then to thermally deposit TPBI as an ETL, LiF as an electron injection layer and Al as a cathode, the samples were loaded into an ultra-high vacuum chamber (~ 10^{-7} Torr). Fabricated PeLEDs were encapsulated with glass lid by using epoxy resin.

2.4. PeLED characterization

Electron current density was recorded using medium-power SMU (Keysight (Agilent) technologies, B1500A). *J-V-L* characteristics were measured using a Keithley 236 as a power source and a Minolta CS-2000 as the EL spectroradiometer.

3. Results and discussion

OHP is easily crystallized during spin-coating because of strong ionic interactions between metal cations and halogen anions [18–20,27]. DMSO is most commonly used to dissolve OHPs. DMSO has relatively low volatility (boiling point ~ 189 °C), so residual DMSO solvent in the perovskite layer dries slowly; as a result, perovskite might be continuously crystallized before the solvent is removed. Therefore, residual solvent should be quickly removed before OHP grains become large. We used a NCP process that uses an electron-transporting TPBI as an additive and CF as a non-polar solvent (Fig. S1a). CF can fully cover the MAPbBr$_3$ film, wash away DMSO solvent, and induce fast co-evaporation with residual DMSO. During A-NCP, TPBI also suppressed continuous crystal growth of MAPbBr$_3$ by intercalating between grains.
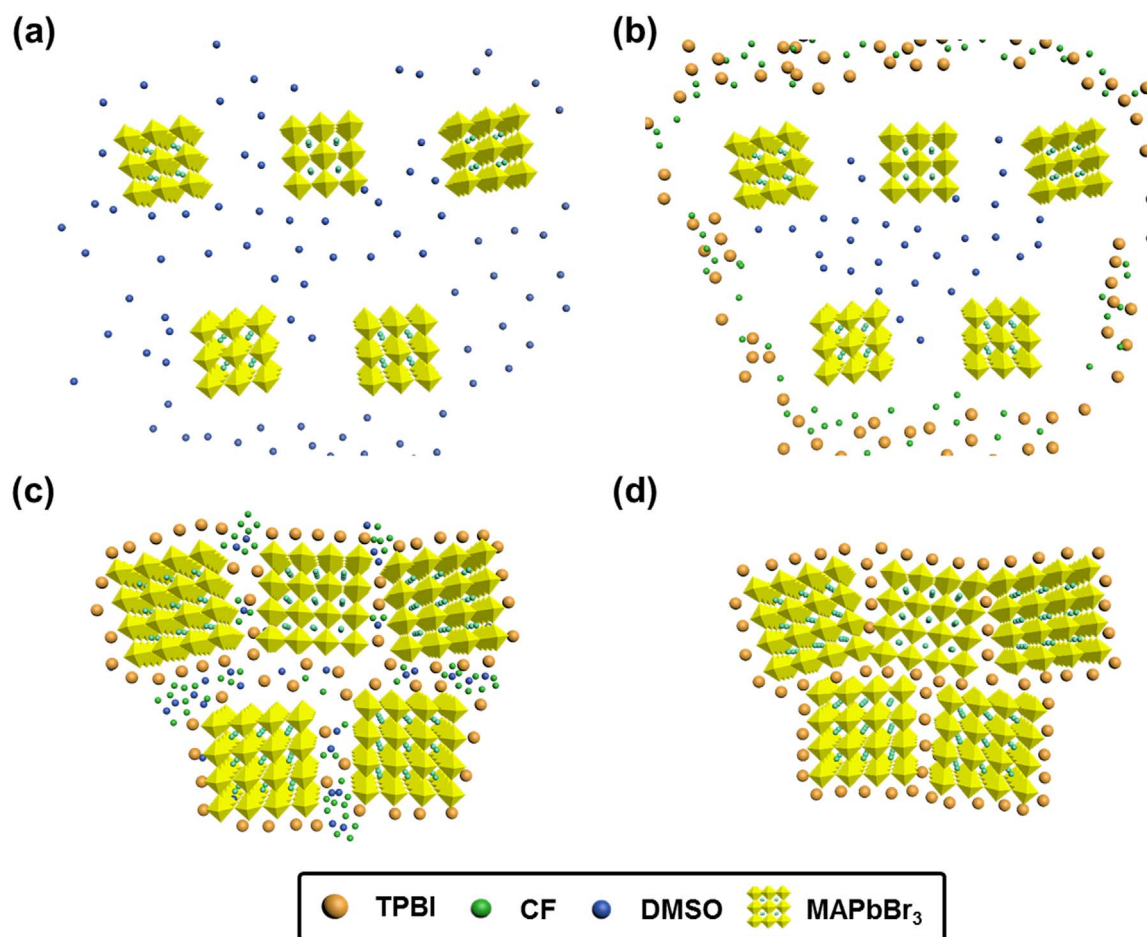
Fig. 1. Schematic mechanism of A-NCP process for MAPbBr$_3$ film formation. (a) Small MAPbBr$_3$ nanocrystals were grown during spin-coating. (b) Spinning MAPbBr$_3$ surface was treated by A-NCP during spin-coating process. (c) TPBI and CF intercalated between grains, and DMSO was rapidly evaporated by volatile CF. (d) MAPbBr$_3$ nanocrystal growth was pinned by TPBI additives.

The schematic mechanism of A-NCP was suggested in Fig. 1 and Supplementary Movie S1. SOCP anode was coated on a glass substrate, then MAPbBr$_3$ was spin-coated as an EML. While MAPbBr$_3$ was spin-coated, solution of x wt% (x = 0, 0.03, 0.05, 0.07, 0.1) TPBI dissolved in CF-treated its surface (Fig. S1b). The reduction of grain size by A-NCP is caused by hindrance of bonding interaction between grains. TPBI in CF more effectively induced smaller grains by being positioned at grain boundaries during continuous crystallization (Fig. 2a). To define the effect of reduced grain size by A-NCP, we measured field-emission SEM (Fig. 2b-f). TPBI-treated MAPbBr$_3$ showed that the grain size of MAPbBr$_3$ decreased as TPBI concentration in CF increased. The grain size distribution of CF-treated MAPbBr$_3$ showed surely broader range from ~ 90 nm to ~ 350 nm (average grain size of CF-treated MAPbBr$_3$ = 171.04 nm), while that of 0.1 wt% TPBI-treated MAPbBr$_3$ was concentrated at around 50–200 nm (average grain size of TPBI-treated MAPbBr$_3$ = 86.67 nm) (Fig. 2g). Moreover, Fig. 2f showed that MAPbBr$_3$ surface and grain boundary areas were slightly covered with TPBI. These changes of surface condition and grain size were also obviously observed from phase images in atomic force microscope (AFM) (Fig. S2). Above all, smooth and TPBI-covered MAPbBr$_3$ surface was clearly observed in the case of 0.1 wt% TPBI.

Supplementary material related to this article can be found online at http://dx.doi.org/10.1016/j.nanoen.2017.10.012.

We also investigated the influence of A-NCP on pristine crystal structure of MAPbBr$_3$ by measuring XRD and XPS. TPBI-treated MAPbBr$_3$ showed identical XRD peaks with CF-treated MAPbBr$_3$ and these patterns are consistent with a stable cubic $Pm\overline{3}m$ phase (Fig. S3) [15]. XPS spectra of Br 3d and Pb 4f core levels were also identical in all

controlled MAPbBr$_3$ (Fig. S4a, b), but the relative intensities sequentially decreased as TPBI concentration increased because the detected amount of TPBI which is located between grains was increased. The XPS N 1s result gave additional evidence that the intensities of detected shoulder peaks by TPBI were increased as the TPBI concentration increased (Fig. S4c). In contrast with Br and Pb, N is common to MAPbBr$_3$ and TPBI. Therefore, the XPS spectra of N 1s core levels from TPBI-treated MAPbBr$_3$ films showed wider and additional XPS peaks (400–401 eV and 398.5 eV) by co-detection of TPBI, and intensities of additional XPS peaks increased as TPBI concentration increased. To define the additional XPS peaks of N 1s from TPBI, N 1s core level spectra of TPBI-treated MAPbBr$_3$ was deconvoluted (Fig. S4d). The XPS spectrum was well fitted into components with peaks at 398.7 eV (pyridinic N), 400.3 eV (pyrollic N), 400.6 eV (pyridonic N), and 401.4 eV (quaternary N), and was well-matched with the N 1s core level spectra of TPBI. Therefore, surface coverage changes and crystal structure analysis results confirmed that TPBI did not affect the crystal structure of MAPbBr$_3$ but was only located at grain boundaries, and that the amount of TPBI at the grain boundaries was increased with depending on the TPBI concentration.

To define the distribution of TPBI in MAPbBr$_3$ film, we conducted the time-of-flight secondary ion mass spectroscopy (TOF-SIMS) measurement (Fig. 3a). First, mass spectra of TPBI were measured to distinguish TPBI additive from MAPbBr$_3$, and the depth profiles of each composition were measured (Figs. S5 and S6). Each TPBI and Pb were measured and we calculated TPBI/Pb ratio to show relative TPBI concentration to MAPbBr$_3$. The TPBI/Pb intensity ratio in pure MAPbBr$_3$ film depicted base line (0 wt% TPBI), and thus we observed relative

(a)

(b) Pure chloroform

200nm

(c) 0.03 wt.% TPBI

200nm

(d) 0.05 wt.% TPBI

200nm

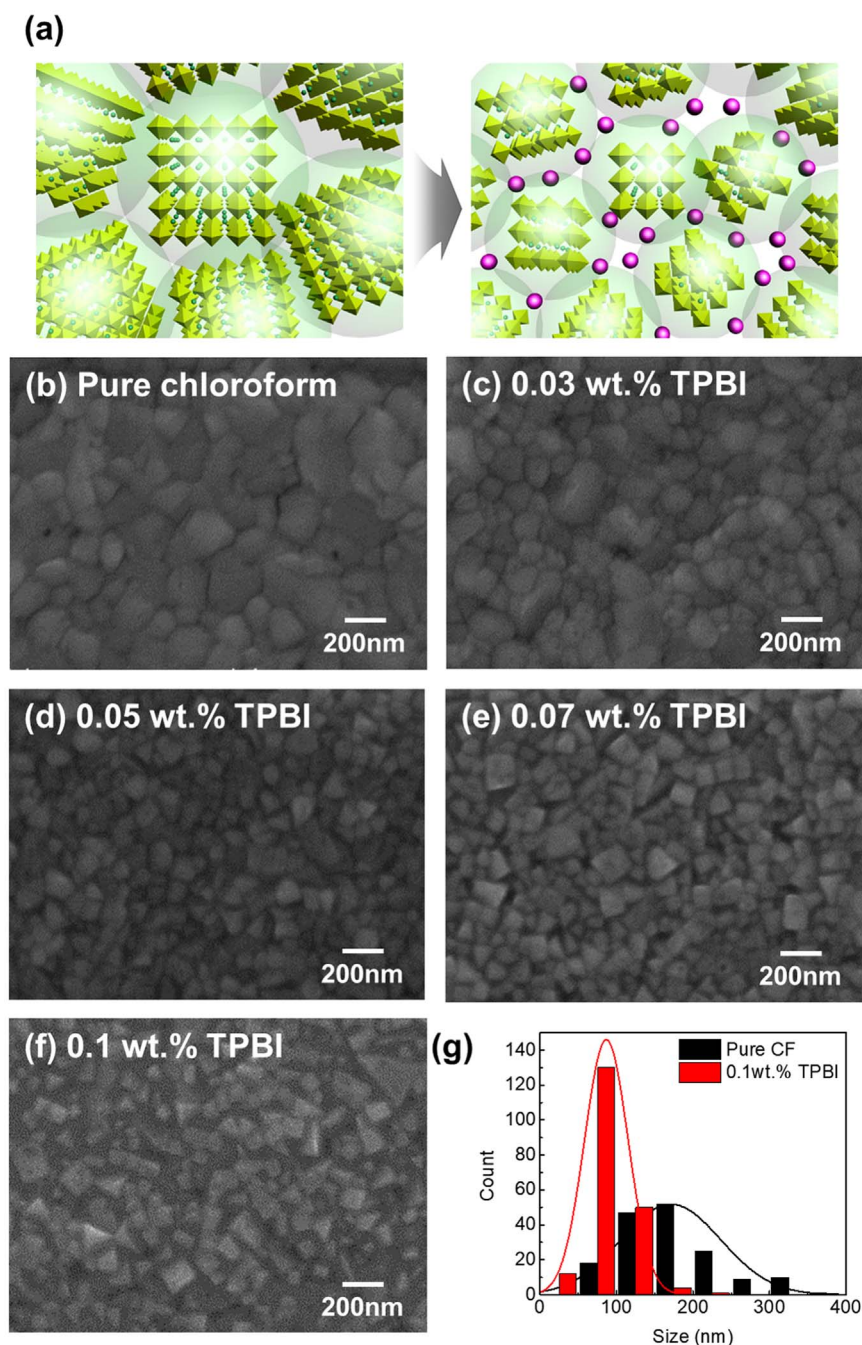**(e) 0.07 wt.% TPBI**

200nm

(f) 0.1 wt.% TPBI

200nm

(g)

Fig. 2. Grain size effect of additives during nanocrystal pinning process (a) Illustration of hindrance effect between grains by A-NCP. (b) SEM image of CF-treated MAPbBr$_3$ film. (c-f) SEM images of TPBI-treated MAPbBr$_3$ films [0.03, 0.05, 0.07, and 0.1 wt% TPBI in CF]. (g) Grain size distribution graph of CF-treated and 0.1 wt% TPBI-treated MAPbBr$_3$ films.

TPBI distribution in 0.1 wt% TPBI-treated MAPbBr$_3$ film. As shown in Fig. 3a, TPBI was mostly concentrated at surface area and it gradually decreased with the depth. We also observed the different steady-state PL intensities at the surface area and bottom face. Because 405 nm excitation wavelength cannot totally penetrate the 400 nm-thick MAPbBr$_3$ film, we can separately observe the PL intensities depending on the direction of exposing light. The sample for PL measurement is sealed with a glass lid, and the glass surface is present on both sides, so that the PL measurement geometry on the top side could be same with that on the bottom side. In the PL intensities of 0.1 wt% TPBI-treated MAPbBr$_3$ (Fig. 3b), higher PL intensity at surface area was measured than that at bottom face. It means that the TPBI-filled MAPbBr$_3$ areas dominantly induced high PL intensity. To investigate the effects of TPBI additives on the recombination rate and a defect healing at grain boundaries, we additionally conducted PL-related measurements. Steady-state PL measurements of TPBI-treated MAPbBr$_3$ film surfaces

showed that the PL intensities gradually increased as TPBI concentration increased from 0 wt% (pure CF) to 0.1 wt% (Fig. 3c). The increased PL intensities of TPBI-treated MAPbBr$_3$ films clearly proved that the radiative recombination rate was increased by exciton confinement effect inside nanograins. Moreover, the non-shifted PL spectra between CF-treated MAPbBr$_3$ and TPBI-treated MAPbBr$_3$ indicates that TPBI additives did not chemically react with traps in bandgap [28]. Therefore, we propose that increased PL intensities of TPBI-treated MAPbBr$_3$ was originated not only from the grain size effect, but also from the defect healing effect, which reduces effective defect density of grain boundaries (Fig. S7).

We conducted TCSPC measurement to understand the defect healing effect and the kinetics of free carriers and excitons, and to quantify the improved radiative recombination rate in detail (Fig. 3d). To avoid other environmental effects on PL lifetime, the MAPbBr$_3$ films were encapsulated with glass lid. We used bi-exponential decay model
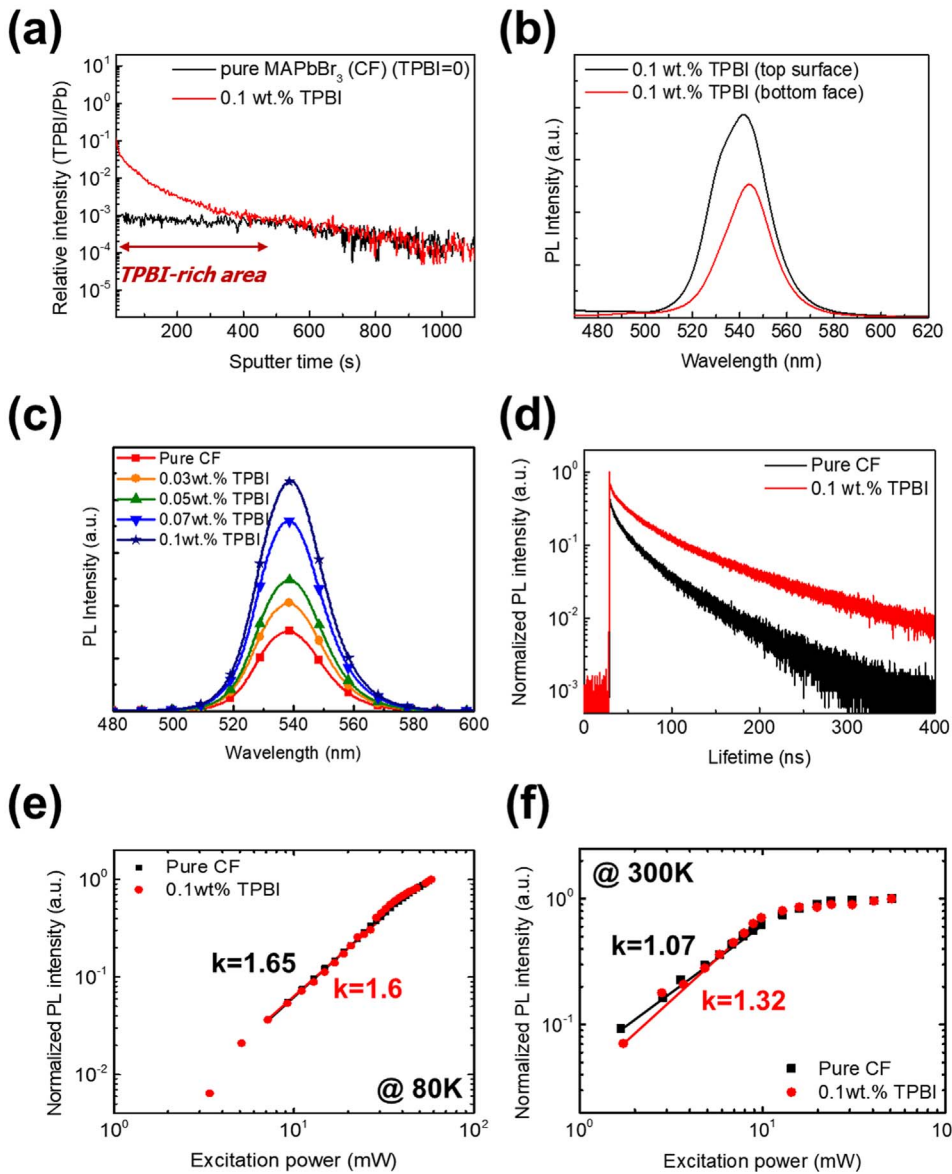
Fig. 3. (a) TPBI distribution profiles calculated by relative TPBI distributions in CF-treated and 0.1 wt% TPBI-treated MAPbBr$_3$ films by measuring time-of-flight secondary ion mass spectroscopy. (b) Steady-state PL intensities of top surface and bottom face of 0.1 wt% TPBI-treated MAPbBr$_3$. (c) Steady-state PL measurements of TPBI-treated MAPbBr$_3$ with 0–0.1 wt% TPBI concentrations. (d) PL lifetime measurement. (e, f) Laser excitation power-dependent PL intensity measurement at 80 K and 300 K.

Table 1
Fast and slow PL lifetime (τ_1, τ_2, ns) and fraction (f_1, f_2, %) calculated using bi-exponential decay model, and average lifetime (τ_{avg}, ns).

MAPbBr$_3$ treatment	τ_1 (ns)	f_1 (%)	τ_2 (ns)	f_2 (%)	$\tau_{average}$ (ns)
Pure CF	17.92	38.26	66.05	61.74	47.63
0.1 wt% TPBI	30.02	34.77	120.69	65.23	89.16

to calculate the PL lifetime (τ) and fraction (f) (Table 1) [15]. The bi-exponential decay model provides two components: one related to trap-assisted non-radiative recombination at grain boundaries (fast-decay component with τ_1 and f_1) and the other one related to radiative recombination inside the grains (slow-decay component with τ_2 and f_2) [15,20]. TPBI-treated MAPbBr$_3$ had τ_1 = 30.02 ns (f_1 = 34.77%) and τ_2 = 120.69 ns (f_2 = 65.23%), while pure CF-treated MAPbBr$_3$ had τ_1 = 17.92 ns (f_1 = 38.26%) and τ_2 = 66.05 ns (f_2 = 61.74%). The decrease in f_1 from CF-treated MAPbBr$_3$ to TPBI-treated MAPbBr$_3$ indicates that fraction of fast decay component decreased; this also means that the effective defect density of grain boundaries was reduced by defect healing effect of A-NCP, so the number of trap-filled charges was reduced and as a result non-radiative recombination rate was decreased.

Moreover, increased f_2 of TPBI-treated MAPbBr$_3$ indicates increase in radiative recombination rate by confining the excitons in nanograins and healing defect of the grain boundaries. The increased contribution of the slow-decay component of PL lifetime from TCSPC measurement agrees well with the increased intensity of steady-state PL.

To study the trap-assisted non-radiative recombination rate in MAPbBr$_3$ with A-NCP, we measured laser excitation power-dependent PL at 80 K and 300 K [29]. At 80 K, thermal energy is too weak to dissociate excitons and activate defects in MAPbBr$_3$, so PL emission is mainly caused by radiative excitonic recombination. Therefore, CF-treated MAPbBr$_3$ and TPBI-treated MAPbBr$_3$ showed almost identical slopes of PL intensity vs. laser excitation power ($k \sim 1.6$, Fig. 3e). With increasing temperature, dissociation of excitons and defects in MAPbBr$_3$ films is thermally-activated and induces trap-assisted recombination, which causes decreases of the slope in power-dependent PL. At 300 K, slopes of both CF-treated and TPBI-treated MAPbBr$_3$ films were decreased ($k \sim 1.07$ for CF-treated MAPbBr$_3$ and $k \sim 1.32$ for TPBI-treated MAPbBr$_3$, Fig. 3f); it means that large decrease amount of the slope in CF-treated MAPbBr$_3$ have large amount of thermally activatable defects. Therefore, this difference indicates that A-NCP effectively healed the effective density of thermally-activatable defects at grain boundaries because TPBI additives were only filled in the grain boundaries.
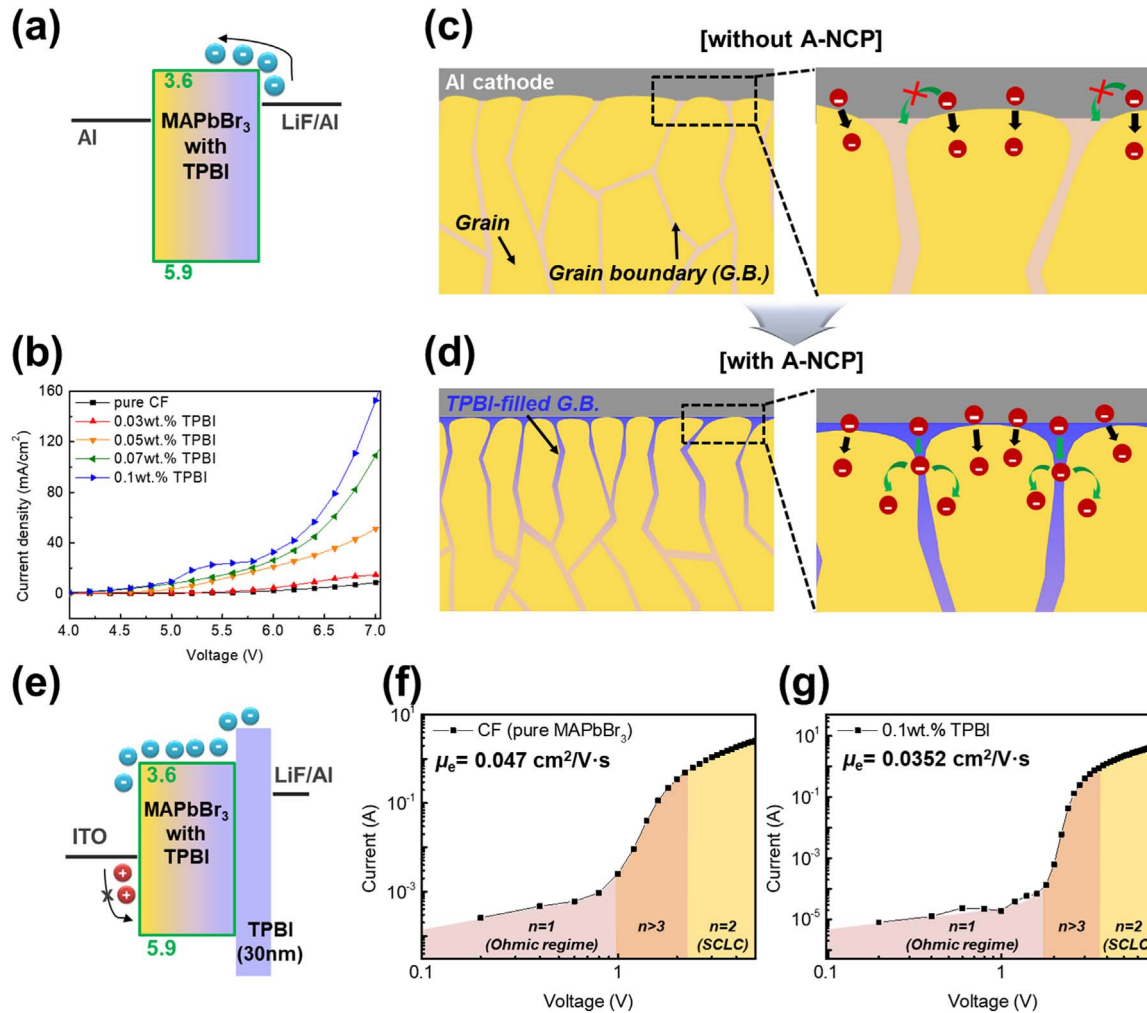
Fig. 4. (a) Device energy diagram for electron injection efficiency measurement. (b) Electron current density-voltage characteristics depending on electron injection property. (c, d) Schematic figures of electron injection efficiency differences in CF-treated and TPBI-treated MAPbBr$_3$. (e) Device structure of electron only devices. (f, g) Space-charge-limited current measurements of CF-treated and 0.1 wt% TPBI-treated MAPbBr$_3$ EODs.

To achieve highly efficient LEDs, balanced electron and hole charges are required in devices. MAPbBr$_3$ shows dominantly p-type behaviour [22,23]. Therefore, the efficient minority electron carrier injection or transport properties in PeLEDs can effectively enhance electron and hole balance in MAPbBr$_3$ EML and thereby increase the fraction of electron-hole pair formation: The charge balance in devices is important because space charges in the devices due to charge imbalance can cause non-radiative recombination such as exciton-charge annihilation, even though one increased radiative recombination rate of electron-hole pairs and decreased trap-assisted non-radiative recombination in the MAPbBr$_3$ films. The improved electron carrier properties in TPBI-treated MAPbBr$_3$ device were investigated by measuring current density-voltage (*J-V*) characteristics of electron injection efficiency-dominated devices and electron-only devices (EODs). Electron injection efficiency measurements were conducted by using the simple devices that are directly deposited the electrode on top of the perovskite surfaces (Fig. 4a). These simple devices were dominantly affected by the electron injection property at the interface between MAPbBr$_3$ and the electrode because other functional layers were not used in the devices. As we confirmed in the results of SEM and AFM, the surface coverage of MAPbBr$_3$ films was gradually changed. Therefore, the gradually increased current densities in Fig. 4b depicted improved electron injection efficiencies by improved surface coverage as TPBI concentration increases. For the intuitive understanding of the improved electron injection efficiency by A-NCP, we illustrated schematic

images (Fig. 4c, d). Without A-NCP, MAPbBr$_3$ surface directly contacted with the electrode, and thus poorly contacted grain boundary areas can act as electron injection barriers. On the other hands, grain boundary areas and grain surfaces were slightly covered with TPBI additives by A-NCP, and thus grain boundary areas can be the electron injection paths. Therefore, improved surface coverage and healed grain boundary areas increased electron injection into the OHP films, and we confirmed that surface grain boundary areas are charge injection barriers. After confirming the improved electron injection efficiencies, we investigated an electron mobility by fabricating the EODs with the structures of ITO/ CF-treated or 0.1 wt% TPBI-treated MAPbBr$_3$/ TPBI (30 nm)/lithium fluoride (LiF) (1 nm)/ Al (100 nm) to define the electrical properties in the bulk MAPbBr$_3$ films (Fig. 4e). The electron mobility was calculated by using Mott-Gurney law, $\mu_e = \frac{8d^3J}{9\varepsilon_0\varepsilon_r V^2}$, in the space-charge-limited current (SCLC) region [d = film thickness, ε_0 = vacuum permittivity, ε_r = 25.5 in MAPbBr$_3$, V = voltage in SCLC region, J = current density in SCLC region] (Fig. 4f, g) [30]. As a result, electron mobility is rather decreased in the case of using A-NCP although the electron mobility of TPBI-treated MAPbBr$_3$ cannot be directly compared to that of CF-treated MAPbBr$_3$ due to difference in grain size and grain boundary area that cause charge transport scattering. It is quite interesting to see the increased radiative recombination in TPBI-treated MAPbBr$_3$ despite larger grain boundary and lower electron mobility than those in CF-treated MAPbBr$_3$, which indicates the healing effect on the grain
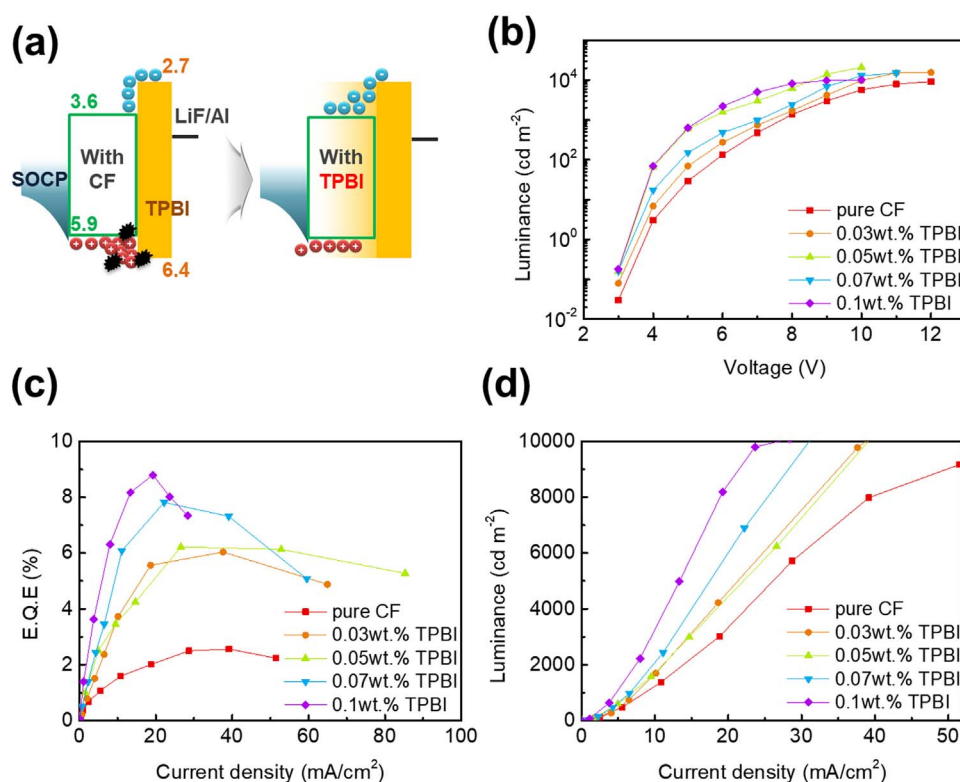
Fig. 5. Device characteristics of TPBI-treated PeLEDs. (a) Schematic images of electron and hole balance in PeLEDs. (b) Luminance-voltage characteristic. (c) External quantum efficiency-voltage characteristic. (d) Luminance-current density characteristic.

boundary by TPBI molecules works for higher radiative recombination; these results of improved electron injection efficiency and grain boundary healing effect for high charge balance in EML and radiative recombination by A-NCP can explain the improved film and device luminescence efficiency.

Finally, we fabricated various PeLEDs fabricated from different TPBI concentration during A-NCP process and characterized their *J-V-Luminance* characteristics (Fig. 5). The structure of PeLEDs was: glass substrate/SOCP (80 nm)/CF-treated or TPBI-treated $MAPbBr_3$ (with TPBI concentrations of 0.03, 0.05, 0.07, 0.1 wt% in CF)/TPBI (50 nm)/ LiF (1 nm)/Al (110 nm). According to the energy-level diagrams and electron transport property improved by A-NCP, we expect that holes were effectively confined in the $MAPbBr_3$ EML by the deep highest occupied molecular orbital (HOMO) level of TPBI (6.4 eV), and that electrons were effectively transported into the $MAPbBr_3$ EML to form a large fraction of electron-hole pairs (Fig. 5a). In CF-treated $MAPbBr_3$ PeLEDs, injected holes accumulate in the $MAPbBr_3$ EML or at the interface between the $MAPbBr_3$ EML and the TPBI ETL (Fig. 5a); therefore, exciton-charge quenching at charge-accumulated region can occur and reduce device efficiency. Operating voltage was reduced when we used A-NCP process for PeLEDs and we also achieved highest external quantum efficiencies (EQEs) of 8.79% from 0.1 wt% TPBI-treated PeLEDs (Fig. 5b, c; Table 2); these results mean that high recombination rate with identical amount of charges (at the same current density) was achieved by 1) increased electron charge density in $MAPbBr_3$ (balanced charges in devices), 2) stronger exciton confinement effect by reduced grain size, and 3) reduced effective defect density of grain boundaries by defect healing effect, and thus it accords with the results that we

suggested above. The 3 major contribution of the TPBI additive in our optimized device structure can explain significantly increased maximum EQE (8.79%) with 0.1 wt%. This result is the highest efficiencies ever reported to date for OHP-based pure green PeLEDs having the Commission Internationale d'Eclairage (CIE) coordinates of (0.27, 0.71) (Fig. S8). Therefore, our elucidation of the role of A-NCP provides clues to boost of PeLED efficiencies and overcomes their limitations.

4. Conclusion

In this study, we noted conventional limitations of PeLEDs such as the low radiative recombination rate and trap-assisted non-radiative recombination in OHP films, and unbalanced charges, which can cause hole accumulation and exciton-charge annihilation, in devices due to dominantly p-type property of $MAPbBr_3$. We elucidated that A-NCP using a tiny amount of electron transporting TPBI as an organic small molecule additive in a volatile non-polar solvent (CF) can resolve these problems in $MAPbBr_3$ films and devices by reducing grain size to confine excitons in nanograins, healing the grain boundaries to reduce effective defect density, and increasing electron injection property to improve charge balance without deteriorating $MAPbBr_3$ structure. These effects of A-NCP during fabrication of OHP EML for PeLEDs explains significant increase of EQE up to 8.79%. Therefore, our work unravels the role of A-NCP process and the resulting electron transporting small molecules positioned at OHP grain boundary areas to increase radiative recombination rate of polycrystalline OHP films in PeLEDs. With this elucidation, A-NCP process may also be used effectively in preparation of other optoelectronic devices that use OHPs.

Table 2
Maximum external quantum efficiencies of TPBI-treated PeLEDs.

	Pure CF	0.03 wt% TPBI	0.05 wt% TPBI	0.07 wt% TPBI	0.1 wt% TPBI
E.Q.E._max [%]	2.56	6.03	6.56	7.81	8.79

Appendix A. Supporting information

Supplementary data associated with this article can be found in the online version at http://dx.doi.org/10.1016/j.nanoen.2017.10.012.

References

[1] N.J. Jeon, J.H. Noh, Y.C. Kim, W.S. Yang, S. Ryu, S.I. Seok, Nat. Mater. 13 (2014) 897–903.

[2] W. Nie, H. Tsai, R. Asadpour, J.C. Blancon, A.J. Neukirch, G. Gupta, J.J. Crochet, M. Chhowalla, S. Tretiak, M.A. Alam, H.L. Wang, A.D. Mohite, Science 347 (2015) 522–525.

[3] F. Deschler, M. Price, S. Pathak, L.E. Klintberg, D.-D. Jarausch, R. Higler, S. Hüttner, T. Leijtens, S.D. Stranks, H.J. Snaith, M. Atatüre, R.T. Phillips, R.H. Friend, J. Phys. Chem. Lett. 5 (2014) 1421–1426.

[4] M. Yuan, L.N. Quan, R. Comin, G. Walters, R. Sabatini, O. Voznyy, S. Hoogland, Y. Zhao, E.M. Beauregard, P. Kanjanaboos, Z. Lu, D.H. Kim, E.H. Sargent, Nat. Nanotechnol. 11 (2016) 872–877.

[5] Y.-K. Chih, J.-C. Wang, R.-T. Yang, C.-C. Liu, Y.-C. Chang, Y.-S. Fu, W.-C. Lai, P. Chen, T.-C. Wen, Y.-C. Huang, C.-S. Tsao, T.-F. Guo, Adv. Mater. 28 (2016) 8687–8694.

[6] A.Y. Chang, Y.-J. Cho, K.-C. Chen, C.-W. Chen, A. Kinaci, B.T. Diroll, M.J. Wagner, M.K.Y. Chan, H.-W. Lin, R.D. Schaller, Adv. Energy Mater. 6 (2016) 1600422.

[7] L.C. Schmidt, A. Pertegas, S.G. Carrero, O. Malinkiewicz, S. Agouram, G.M. Espallargas, H.J. Bolink, R.E. Galian, J.P. Prieto, J. Am. Chem. Soc. 136 (2014) 850–853.

[8] Z.-K. Tan, R.S. Moghaddam, M.L. Lai, P. Docampo, R. Higler, F. Deschler, M. Price, A. Sadhanala, L.M. Pazos, D. Credgington, F. Hanusch, T. Bein, H.J. Snaith, R.H. Friend, Nat. Nanotechnol. 9 (2014) 687–692.

[9] J. Byun, H. Cho, C. Wolf, M. Jang, A. Sadhanala, R.H. Friend, H. Yang, T.-W. Lee, Adv. Mater. 28 (2016) 7515–7520.

[10] Y.-H. Kim, H. Cho, T.-W. Lee, Proc. Natl. Acad. Sci. 113 (2016) 11694–11702.

[11] Y.-H. Kim, H. Cho, J.H. Heo, T.-S. Kim, N. Myoung, C.L. Lee, S.H. Im, T.-W. Lee, Adv. Mater. 27 (2015) 1248–1254.

[12] R.L.Z. Hoye, M.R. Chua, K.P. Musselman, G. Li, M.-L. Lai, Z.-K. Tan, N.C. Greenham, J.L. MacManus-Driscoll, R.H. Friend, D. Credgington, Adv. Mater. 27 (2015) 1414–1419.

[13] S. Gonzalez-Carrero, R.E. Galian, J. Pérez-Prieto, J. Mater. Chem. A 3 (2015) 9187–9193.

[14] V. D'Innocenzo, A.R.S. Kandada, M.D. Bastiani, M. Gandini, A. Petrozza, J. Am. Chem. Soc. 136 (2014) 17730–17733.

[15] H. Cho, S.-H. Jeong, M.-H. Park, Y.-H. Kim, C. Wolf, C.-L. Lee, J.H. Heo, A. Sadhanala, N.S. Myoung, S. Yoo, S.H. Im, R.H. Friend, T.-W. Lee, Science 350 (2015) 1222–1225.

[16] N.K. Kumawat, A. Dey, A. Kumar, S.P. Gopinathan, K.L. Narasimhan, D. Kabra, ACS Appl. Mater. Interfaces 7 (2015) 13119–13124.

[17] G. Xing, N. Mathews, S. Sun, S.S. Lim, Y.M. Lam, M. Gratzel, S. Mhaisalkar, T.C. Sum, Science 342 (2013) 344–347.

[18] Q. Dong, Y. Fang, Y. Shao, P. Mulligan, J. Qiu, L. Cao, J. Huang, Science 347 (2015) 967–970.

[19] S.D. Stranks, G.E. Eperon, G. Grancini, C. Menelaou, M.J.P. Alcocer, T. Leijtens, L.M. Herz, A. Petrozza, H.J. Snaith, Science 342 (2013) 341–344.

[20] D. Shi, V. Adinolfi, R. Comin, M. Yuan, E. Alarousu, A. Buin, Y. Chen, S. Hoogland, A. Rothenberger, K. Katsiev, Y. Losovyj, X. Zhang, P.A. Dowben, O.F. Mohammed, E.H. Sargent, O.M. Bakr, Science 347 (2015) 519–522.

[21] J.J.M. van der Holst, F.W.A. van Oost, R. Coehoorn, P.A. Bobbert, Phys. Rev. B 80 (2009) 235202.

[22] T. Shi, W.-J. Yin, F. Hong, K. Zhu, Y. Yan, Appl. Phys. Lett. 106 (2015) 103902.

[23] A. Buin, R. Comin, J. Xu, A.H. Ip, E.H. Sargent, Chem. Mater. 27 (2015) 4405–4412.

[24] J. Kalinowski, W. Stampor, J. Szmytkowski, D. Virgili, M. Cocchi, V. Fattori, C. Sabatini, Phys. Rev. B 74 (2006) 085316.

[25] X.Y. Chin, D. Cortecchia, J. Yin, A. Bruno, C. Soci, Nat. Commun. 6 (2015) 7383.

[26] J.G. Labram, D.H. Fabini, E.E. Perry, A.J. Lehner, H. Wang, A.M. Glaudell, G. Wu, H. Evans, D. Buck, R. Cotta, L. Echegoyen, F. Wudl, R. Seshadri, M.L. Chabinyc, J. Phys. Chem. Lett. 6 (2015) 3565–3571.

[27] Z. Xiao, Q. Dong, C. Bi, Y. Shao, Y. Yuan, J. Huang, Adv. Mater. 26 (2014) 6503–6509.

[28] Y. Shao, Z. Xiao, C. Bi, Y. Yuan, J. Huang, Nat. Commun. 5 (2014) 5784.

[29] T. Schmidt, K. Lischka, W. Zulehner, Phys. Rev. B 45 (1992) 8989–8994.

[30] M.I. Saidaminov, A.L. Abdelhady, B. Murali, E. Alarousu, V.M. Burlakov, W. Peng, I. Dursun, L. Wang, Y. He, G. Maculan, A. Goriely, T. Wu, O.F. Mohammed, O.M. Bakr, Nat. Commun. 6 (2015) 7586.

Min-Ho Park received his M.S. (2013) and Ph.D. (2017) in department of Material Science and Engineering from Pohang University of Science and Technology (POSTECH), Republic of Korea and his B.S. (2011) in department of Material Science and Engineering from Inha University, Republic of Korea. His research interests include vacuum- or solution-processed light-emitting diodes by using the organic or organic-inorganic perovskite materials for displays and solid-state lightings.

Su-Hun Jeong received his B.S. (2012) and Ph.D. (2017) in Materials Science and Engineering from Pohang University of Science and Technology (POSTECH), Republic of Korea. His current research work is focused on polymeric electrodes for flexible organic and perovskite optoelectronic devices.
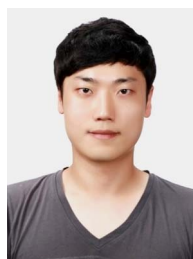
Hong-Kyu Seo received his Ph.D. (2017) in Division of Environmental Science and Engineering from Pohang University of Science and Technology (POSTECH), Korea. He is currently working in Samsung Advanced Institute of Technology (SAIT), Korea as a senior researcher. His research focuses on graphene electronics and organic-inorganic hybrid materials for flexible displays and solid-state lightings.

Christoph Wolf received his B.S. and M.S. in Engineering Physics from University of Technology Graz, Austria. He is currently finishing his Ph.D. studies in the department of Materials Science and Engineering at Pohang University of Science and Technology (POSTECH). His studies focus on spectroscopy and first-principles calculation of novel semiconductor materials for opto-electronic applications.

Young-Hoon Kim received his M.S. (2014) in Division of Environmental Science and Engineering and Ph.D. (2016) in Material Science and Engineering from Pohang University of Science and Technology (POSTECH), Korea. He is currently working in Materials Science and Engineering at Seoul National University, Korea as a post-doctoral researcher (2016–2017). His research focuses on solution-processed electronics based on organic and organic-inorganic hybrid materials for flexible displays and solid-state lightings.

Hobeom Kim received his Ph.D. (2017) in the Department of Materials Science and Engineering at Pohang University of Science and Technology (POSTECH), Republic of Korea. He received his B.S. in the School of Advanced Materials Science and Engineering from Sungkyunkwan University (SKKU), Korea in 2011. His current research activity is focused on organic and metal halide perovskite optoelectronics.

Himchan Cho received his B.S. (2012.02) and Ph.D. (2016.08) in Materials Science and Engineering from Pohang University of Science and Technology (POSTECH), Republic of Korea. He is currently working as a postdoctoral researcher at Seoul National University, Republic of Korea (2016.09-current). His research interests include organic/inorganic hybrid electronics, organic/polymer electronics, organic nanowire printing/electronics, photophysics in semiconducting materials and electronic devices.

Jinwoo Byun received his M.S. (2016) in Materials Science and Engineering, Pohang University of Science and Technology (POSTECH), Korea. Now he is a Ph.D. candidate at Materials Science and Engineering, Korea Advanced Institute of Science and Technology (KAIST), Korea. His research interests mainly focus on 2D & quasi-2D perovskite materials.

Tae-Woo Lee is an associate professor in Materials Science and Engineering at Seoul National University, Korea. He received his Ph.D in Chemical Engineering from KAIST, Korea in 2002. He joined Bell Laboratories, USA as a postdoctoral researcher and worked in Samsung Advanced Institute of Technology as a member of research staff (2003–2008). He was an associate professor in Materials Science and Engineering at Pohang University of Science and Technology (POSTECH), Korea until Aug, 2016. His research focuses on printed electronics based on organic and organic-inorganic hybrid materials for flexible displays, solid-state lightings, and solar-energy-conversion devices.

Joo Sung Kim received his B.S. in Materials Science and Engineering from Pohang University of Science and Technology (POSTECH) in 2016. He is currently pursuing his integrated Ph.D. in Materials Science and Engineering at Seoul National University(SNU). His research interests include organic/inorganic hybrid optoelectronics, organic light emitting diodes and spectroscopy.